

Key Points:

- The statistical funnel of deep-ocean sediment traps is mainly determined by mesoscale dynamics in the twilight zone
- On average the vertical flow enhances particle sinking, but with more variance in spring than in other seasons
- Coherent eddies reduce the particle dispersion within a local area, with vertical acceleration (deceleration) by anticyclones (cyclones)

Supporting Information:

Supporting Information may be found in the online version of this article.

Correspondence to:

L. Wang,
Lu.Wang@univ-brest.fr

Citation:

Wang, L., Gula, J., Collin, J., & Mémery, L. (2022). Effects of mesoscale dynamics on the path of fast-sinking particles to the deep ocean: A modeling study.

Journal of Geophysical Research: Oceans, 127, e2022JC018799. <https://doi.org/10.1029/2022JC018799>

Received 11 MAY 2022

Accepted 8 JUL 2022

Effects of Mesoscale Dynamics on the Path of Fast-Sinking Particles to the Deep Ocean: A Modeling Study

Lu Wang¹ , Jonathan Gula^{2,3} , Jérémie Collin¹, and Laurent Mémery¹ 

¹University Brest, CNRS, IRD, Ifremer, Laboratoire des Sciences de l'Environnement Marin (LEMAR), IUEM, Plouzané, France, ²University Brest, CNRS, IRD, Ifremer, Laboratoire d'Océanographie Physique et Spatiale (LOPS), IUEM, Plouzané, France, ³Institut Universitaire de France (IUF), Paris, France

Abstract The gravitational sinking of organic particles is a vital component of the biological carbon pump. This sinking process is strongly modulated by the spatiotemporally varying eddy field, complicating the interpretation of particle flux measured by deep-moored sediment traps. By backtracking particles to 200 m depth based on the outputs of a realistic eddy-resolving simulation, we characterize the origins of particles collected at a long-term observatory site in the Northeast Atlantic and focus on the impact of mesoscale dynamics on particle transport. Our results show that mesoscale dynamics between 200 and 1,000 m control the statistical funnel. Over the long term, the horizontal sampling scales of traps are estimated as hundreds of kilometers, with containment radius ranging from 90 to 490 km, depending on sinking velocities. Particle travel time suggests that overall vertical flow acts to facilitate the export, with estimated deviations up to 1 ± 2 days for particles sinking at 50 m d^{-1} to 1,000 m. Statistical analyses of horizontal displacements reveal that mesoscale eddies at the site confine particle sources in a more local area. On average, particles in anticyclonic eddies sink faster to depth than expected from purely gravitational sinking, contrary to their counterparts in cyclonic eddies. The results highlight the critical role of mesoscale dynamics in determining particle transport in a typical open ocean region with moderate eddy kinetic energy. This study provides implications for the sampling design of particle flux measurements during cruises and the interpretation of deep-ocean mooring observations.

Plain Language Summary As plants in the ocean, phytoplankton organisms transform the atmospheric CO₂ into organic carbon that forms particles of various sizes sinking to the deep ocean due to gravity. The falling particles can be collected by containers called sediment traps. However, particles may originate far from the surface ocean directly above the trap as ocean currents horizontally transport particles. Also, the time taken by particles to sink to the deep ocean varies due to vertical motions of seawater. To study the impact of ocean currents on sinking particles, we use an ocean model and virtual particles. We release particles at a fixed location, representing a sediment trap, and track particle trajectories back in time to identify their source regions. Our results show that the size of this source region is mainly determined by currents between 200 and 1,000 m. On average, particles tend to sink faster than expected from purely gravitational sinking. Large whirlpools of water above the trap lead to a local source region, which suggests that the particle flux can be better correlated to the surface production of organic carbon in this case. The finding has implications for the sampling strategy and the interpretation of particle export measurements in regional surveys.

1. Introduction

A vital process of oceanic carbon cycling is the biological carbon pump (BCP) which sequesters atmospheric CO₂ by exporting photosynthetically produced organic carbon from the surface layer to the deep ocean (Falkowski et al., 1998). The BCP is mainly regulated by the sinking particulate organic carbon (POC) produced in the euphotic zone (Henson et al., 2015; Riley et al., 2012; Sanders et al., 2014; Turner, 2015). Long-term observations of the downward particle flux are available from moored sediment traps over recent decades (Buesseler et al., 2007; Lampitt & Antia, 1997; Lampitt et al., 2010; Le Moigne et al., 2013). Traditionally, POC export through gravitational sinking is evaluated from a quasi-one-dimensional (1D) viewpoint, which couples particle interception by sediment traps with particle production in the surface ocean directly above the trap (Armstrong et al., 2001; Asper et al., 1992; Deuser & Ross, 1980). However, particles are also affected by horizontal advection during their vertical sinking (Burd et al., 2010; Deuser et al., 1990; Siegel et al., 1990). Consequently,

impacts of hydrodynamics on sinking particles challenge the link of particle collection at depth with surface signatures (Dever et al., 2021), and hence promote the extrapolation of POC export in a spatiotemporally varying circulation field.

The concept of the statistical funnel has been raised to construct a dynamical source region enclosing the likely origins of particles settling to time-series sediment traps (Siegel & Deuser, 1997). The statistical funnel is often characterized by analyzing Lagrangian particles backtracked from the trap location to the surface ocean. Waniek et al. (2000) identified origins of particles from separated, distant regions by daily mean observed current profiles at a quasi-time-series station in the northeast Atlantic. Siegel et al. (2008) constructed statistical funnels for a deep-moored trap in the Pacific ocean using a combination of satellite-derived geostrophic velocities and ship-board ADCP profiles. They estimated horizontal scales larger than 300 km for a trap at 4,000 m collecting particles sinking at 50 m d⁻¹. Such a sampling scale is confirmed by Qiu et al. (2014) with the use of a time-dependent 3D velocity field of a circulation model. Furthermore, studies of Liu et al. (2018) and Wekerle et al. (2018) both showed that the statistical funnels vary with the trap location and seasons, and highlighted the presence of eddies in determining the particle sources. These studies have shown that the statistical funnel of moored sediment traps depends on trap depth, particle sinking velocity, collection time, and regional advective processes.

Ocean mesoscale dynamics exert influences on POC export by generating a heterogeneous distribution of primary production that produce sinking particles (Lévy et al., 2018; Mahadevan, 2016), and by directly modulating particle transport (Boyd et al., 2019). Mechanisms of the physical-biological interactions at mesoscale have been demonstrated in terms of eddy stirring, trapping, and pumping (McGillicuddy, 2016; McWilliams, 2008; Olson, 1991). Eddies can horizontally advect and diffuse particles (Deuser et al., 1988; Siegel et al., 1990, 2008), and add an additional advective vertical flux of POC in the eddy-related frontal region (Stukel et al., 2017). Also, eddies can structure the subsurface distribution of particles, leading to a deep-reaching funnel of particles toward the eddy center (Waite et al., 2016). Furthermore, mesoscale dynamics may have an impact on the POC export at smaller scales (Klein & Lapeyre, 2009). In the horizontal, strong surface convergent zones associated with submesoscale cyclonic fronts are found to concentrate materials into tight clusters within a short time (D'Asaro et al., 2018; McGillicuddy, 2016; Poje et al., 2014), leading to a preferred accumulation of buoyant material into mesoscale cyclones (Vic et al., 2022). While in the vertical, large vertical velocities generated at submesoscale frontal structures extend from the surface down to hundreds of meters (Klein & Lapeyre, 2009; Lévy et al., 2012; Mahadevan & Tandon, 2006). The magnitude of vertical velocity in different dynamical regimes ranges from $\mathcal{O}(10)$ to $\mathcal{O}(100)$ m d⁻¹ (Pietri et al., 2021), comparable to the majority of particle sinking velocities accounting for carbon fluxes at depth (50–200 m d⁻¹) (Turner, 2002). The control of vertical flows on the travel time of particles is important for sediment trap measurements, especially during the period of rapid spring blooms (Asper et al., 1992). In this manner, the local vertical velocity field may considerably affect particle export from the upper ocean. Observations have shown elevated POC flux generated by the stretching features in the frontal region between mesoscale eddies (Guidi et al., 2012). The elevations were mostly detected within the mixed layer, though the mixed layer base did not appear to obstruct the particle export. Intensified mesoscale eddies may also produce deep-reaching submesoscale fronts that penetrate well below the mixed layer (Siegelman et al., 2020; Yu et al., 2019). Such findings suggest enormous potential impacts of mesoscale eddies and their associated submesoscale dynamics on the fate of particle export to the deep ocean.

As an interface between the well-studied epipelagic layer (sunlight zone) and the dark deep ocean, the mesopelagic layer (also known as the “twilight zone”) spanning from 200 to 1,000 m is a crucial element in the rapid removal of carbon further down to the deep ocean. However, the understanding of the role of the twilight zone in carbon transport remains to be improved from physical, biogeochemical, and ecological perspectives (Martin et al., 2020). Since 2019, the Joint Exploration of the Twilight Zone Ocean Network (JETZON) has been set up to provide a new scientific understanding of the twilight zone. It coordinates a variety of international projects, one of which is the French project Assessing marine biogenic matter Production, Export and Remineralization from the surface to the dark Ocean (APER), built on an upcoming intensive field program at the Porcupine Abyssal Plain sustained observatory (PAP-SO) in the open-ocean region of Northeast Atlantic. The PAP site allows simultaneous studies of both upper ocean and abyssal depths, where deep-sea POC flux has been measured over decades using a long-term sediment trap mooring. Scheduled for June 2023 when the export peaks, the cruise of APER follows the US EXPORTS cruise to the same location during the bloom/post-bloom period in May 2021 (Siegel et al., 2016).

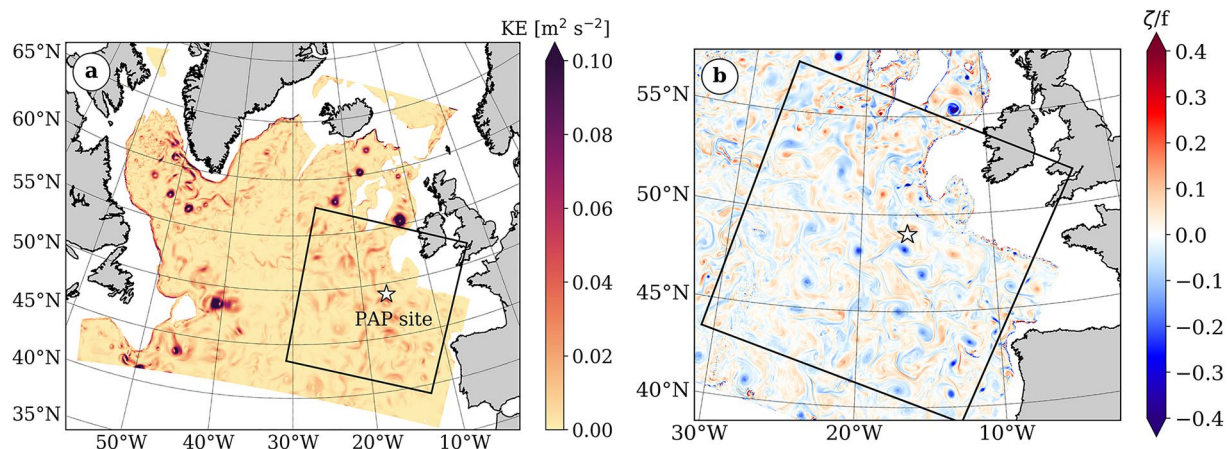


Figure 1. Snapshots of (a) kinetic energy at 1,000 m for the whole POLGYR domain and (b) a zoomed relative vorticity field at 1,000 m. The study region is in the black box centered on the Porcupine Abyssal Plain site (white star).

Motivated by the sustained observations and upcoming APERO cruise in the PAP region, this study aims to identify the source region of particles collected by deep-ocean sediment traps, and investigate how mesoscale patterns shape the statistical funnel of particles. We use outputs from an eddy-resolving regional ocean model to backtrack particles from the PAP site. The findings will have implications for the design of the Process Study Stations to be deployed during the APERO cruise. This work assesses for the first time the impact of small/medium-scale dynamics on the dispersion of sinking particles in the mesopelagic layer (200–1,000 m), once exported below the surface mixed layer. The paper is organized as follows. Section 2 provides information on the ocean circulation simulations and Lagrangian experiment design. Section 3 presents results of particle backtracking, including statistical funnels, horizontal and vertical dispersion, and the role of specific flow structures on particle transport. Finally, we offer conclusions and discussion on the findings in Section 4.

2. Experiment Setup

The particle backtracking experiments are designed to reconstruct a large number of particle trajectories from sediment trap locations to the upper boundary of the twilight zone. Our goals are to characterize statistical funnels of deep-ocean sediment trap sampling, and to relate their spatio-temporal variability to underlying mesoscale dynamics.

2.1. Numerical Model Outputs

Instantaneous outputs at 12 hourly intervals from a realistic eddy-resolving model are used to compute particle trajectories. The simulation was performed using Coastal and Regional Ocean Community model (CROCO) built upon ROMS (Shchepetkin & McWilliams, 2005) which solves the hydrostatic primitive equations for the momentum and state variables. The configuration (POLGYR) has $2,000 \times 1,600$ grid points covering the North Atlantic Subpolar Gyre. The horizontal grid spacing is 2 km, much smaller than the first Rossby deformation radius over this domain (10–20 km) (Chelton et al., 1998). There are 80 vertical sigma levels, with a variable resolution following the topography (about 5 m at the surface and 40 m at the bottom, up to 100 m for the maximum vertical spacing in the intermediate layer). After a two-year spin-up time, the simulation is run from 2001 to 2009, and we use the seven years between 2002 and 2008. The use of 12-hourly wind forcing and the absence of tides largely reduces the generation of internal waves and high-frequency variability.

Le Corre et al. (2020) provide a detailed description of the simulation, and validation through comparisons of the mean circulation as well as mesoscale activity, with observations from drifters and Argo floats. In this study, we focus on the southeastern portion of the whole domain, with a size of $1,600 \times 1,600$ km centered on the PAP site (49°N , 16.5°W). The study region is characterized by moderate kinetic energy compared to the western and northern parts of the subpolar gyre (Figure 1a). The mean flow in this region is around 0.05 m s^{-1} (Le Cann, 2005); such a weak advection enables particles initially seeded at the PAP site to stay within this subdomain for several

months. The circulation in this region is dominated by mesoscale eddy activity. A stream of cyclonic and anticyclonic eddies intermittently crosses the PAP site (Figure 1b), feeding the site with an eastward meandering North Atlantic Current branch, and flows from the European shelf (Hartman et al., 2010).

2.2. Lagrangian Particle Tracking

We use a Python/Fortran hybrid parallelized code, named “Pyicles” (Gula & Collin, 2021), to track offline particles backward to their source locations. Particles evolve in the native Arakawa C-grid and terrain-following vertical coordinates of the ocean model. The model fields are linearly interpolated at particle positions in space and time. The numerical time scheme for advection is Runge-Kutta 4, with a time step of 2 min, which ensures that the Courant-Friedrichs-Lowy condition is satisfied. The Lagrangian model has a good performance in the reversibility of particle tracking, with errors of $\mathcal{O}(10^{-4})$ m for horizontal displacement and $\mathcal{O}(10^{-7})$ m for vertical displacement, over a travel distance of $\mathcal{O}(10)$ km. Sensitivity tests verified that increasing the frequency of CROCO snapshots used for experiments from 12 to 1 hr, or using averages instead of snapshots, has a negligible impact on the statistical results of particle dispersion (Figure S1 in Supporting Information S1) and vertical velocities (Figure S2 in Supporting Information S1). Therefore, 12 hr instantaneous outputs are sufficient to capture particle dynamics for such a typical open-ocean region where mesoscale currents dominate, and sources of high-frequency variability such as submesoscale currents and internal waves are not fully resolved.

A series of experiments is performed to backtrack particles monthly collected over the seven years (2002–2008). The seeding depths are chosen at 1,000 and 2,000 m, representing the bottom of the twilight zone and a standard depth of the deep-ocean sediment traps, respectively. This study focuses on the impact of mesoscale dynamics in the mesopelagic layer once particles are exported below the mixed layer. Hence the base of the epipelagic layer, 200 m, is chosen as the end depth where source locations of particles are determined. This depth is also a typical depth of the deep winter mixed layer in this region (Coatanoan, 2021; Yu et al., 2019). Four constant sinking speeds (200, 100, 50, and 20 m d⁻¹) are assigned to particles. They are mostly endorsed by observations at the PAP site giving the range of particle sinking rates from 30 m d⁻¹ (Villa-Alfageme et al., 2014) to 180 m d⁻¹ (Riley et al., 2012). Particles are initialized every 12 hr within a 10 × 10 km seeding patch centered on the PAP site, corresponding to 6 × 6 grid points with one particle located at each grid point. The choice of the patch size implicitly considers the dispersion due to subgrid-scale mixing, as there is no parameterized diffusivity in the Lagrangian model. We have tested that the exact location of the particles inside the patch does not impact our results by performing additional experiments with particles randomly seeded in the patch (not shown). In each experiment, particles are injected continuously every 12 hr over one month and are tracked until they reach 200 m. The total number of particles for a monthly analysis is 2,160 (i.e., 36 × 60).

To investigate how the dynamical regimes of horizontal advection change with depth, we also deploy depth-keeping particles on the horizontal plane at different depths. The seeding patch and the timing of particle release in these 2D experiments are the same as in the 3D ones.

3. Results

3.1. Statistical Funnel of Deep-Ocean Sediment Traps

3.1.1. Overview of the Source Regions

The distribution of particle source regions at 200 m shows a synoptic picture of the sampling area resulting from the integrated horizontal advection over time and space (Figure 2). Mesoscale eddies transport particles from distant regions to the PAP site, which forms a diffuse cloud of particle sources at the export depth. Such an effect has been indicated in Vic et al. (2018) by comparing the dispersion pattern driven by mesoscale currents to that by the mean flow. The sensitivity experiments here indicate that the catchment area of a moored sediment trap increases with the trap depth (top panel vs. bottom panel) and decreases with particle sinking velocity (e.g., from (a) to (d) on the top panel). Qualitatively, changes in the sampling area with sinking velocity are more significant than changes due to the trap depth. The area with particle density exceeding 10^{-2%} for 2,000 m trap remains almost the same as for the 1,000 m trap, whereas the radius of this area reduces by hundreds of kilometers when particle sinking velocity increases from 20 to 200 m d⁻¹. It suggests that the dynamics between 1,000 and 2,000 m does not effectively alter the statistical funnel as much as that in the twilight zone (200–1,000 m).

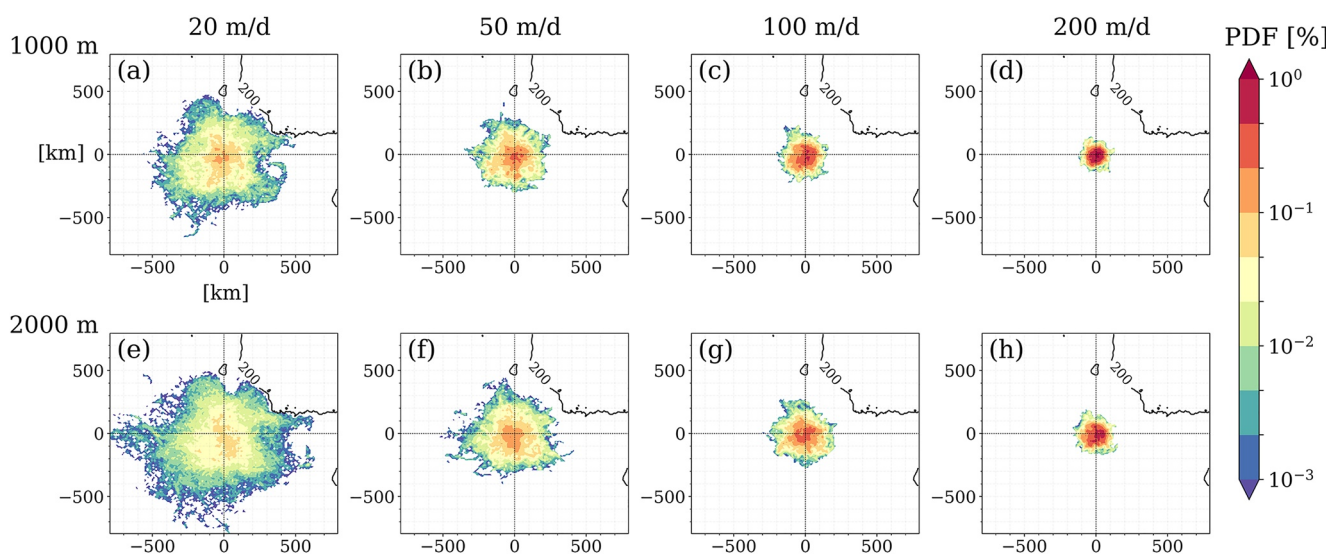


Figure 2. Source region at 200 m for particles collected by the moored sediment traps over the seven years (2002–2008), with different sinking velocities from two trap depths (a–d, 1,000 m; e–h, 2,000 m). Particle positions are binned into a 10 km × 10 km grid. The color indicates the percentage, that is, the number of particles in each bin divided by the total amount of particles. The black contour is the 200 m isobath.

The source regions are further quantified using a set of basic metrics (Table 1). Mean displacements (r_{mean}) range from 47 to 190 km for the collection at 1,000 m, with only a modest increase of <50 km for the collection at 2,000 m. The collection scale of deep-moored sediment traps is as large as 100 km, even for fast-sinking particles. Containment radii ($R_{95\%}$), defined as the radial distance covering 95% of a source region, are 90 and 118 km for particles sinking velocity of 200 m/d. The $R_{95\%}$ dramatically increases as the sinking velocity decreases, with the largest value of 490 km for particles sinking at 20 m d⁻¹ to the trap at 2,000 m. Our estimates of the mean displacement and containment radii are much larger than the estimates obtained by Siegel et al. (2008) due to the higher-resolution velocity field and the larger subsurface EKE in our study region. The percentage of area with probability densities larger than 10⁻²% confirms that changes of source area with sinking velocity are more significant than with trap depths.

Figure 3 shows the vertical structure of statistical funnels by integrating trajectories of particles from 2000 m projected on the zonal section. The funnels of particles sinking at 100 m d⁻¹ and 200 m d⁻¹ have limited widths with less variability over depth. By contrast, the collection of the two slower sinking classes is primarily controlled by the dynamics changing with depth, especially the twilight zone, as indicated by the widened bounds. The broadening of funnels between 200 and 1,000 m coincides with vertical profiles of eddy kinetic energy (EKE) and root-mean-square vertical velocity w_{rms} (Figures 3e and 3f). The former indicates horizontal transport, while the latter influences the shape of statistical funnels by affecting the sinking time of particles. The magnitude of EKE and w_{rms} are comparable to the OSMOSIS mooring observations (Yu et al., 2019). EKE shows a rapid decay from over 100 cm² s⁻² in the upper ocean, down to 20 cm² s⁻² at 1,000 m, and remains at such low level from here. The vertical velocity w_{rms} is intensified up to 40 m d⁻¹ at 200 m during winter months when submesoscale motions are active, and at around 20 m d⁻¹ for autumn and summer when mesoscale activity dominates. The slight linear increase of w_{rms} with depth below 1,000 m corresponds to a bottom intensification of vertical flows due to interactions with topography. As such, the influence of vertical flows is considerable for the 20 and 50 m d⁻¹ particle groups. Based on the two profiles, the water column below the epipelagic layer can be divided into three layers with different regimes: Energetic layer (200–500 m) with high EKE and large w_{rms} , Active layer (500–1,000 m) with

Table 1
Quantitative Information for Particle Source Regions

Depth [m]	w_{sed} [m d ⁻¹]	r_{mean} [km]	$R_{95\%}$ [km]	$S_{PDF>10^{-2}\%}$ [%]
1,000	20	190	394	41.6
1,000	50	116	230	62.5
1,000	100	76	146	72.8
1,000	200	47	90	80.7
2,000	20	236	490	31.4
2,000	50	141	280	52.6
2,000	100	96	194	66.1
2,000	200	64	118	76.8

Note. The left two columns list trap depths and particle sinking velocities. The right three columns are mean displacement (r_{mean}), the radial distance containing 95% of the source region ($R_{95\%}$), and the percentage of source area with PDF larger than 10⁻²%, respectively.

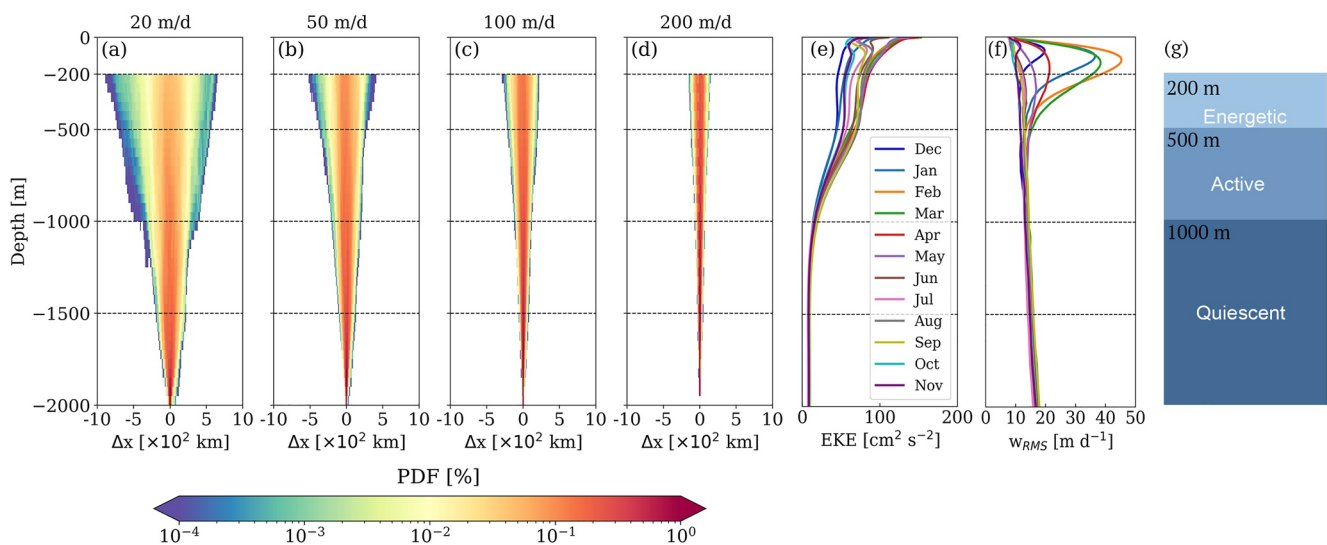


Figure 3. (a–d) Seven-year integrated particle trajectories backtracked from 2000 m, projected on the zonal section with a bin size of $10 \text{ km} \times 50 \text{ m}$. The color indicates the percentage, that is, the number of particles in each bin divided by the total amount of particles (e and f) Vertical profiles of monthly climatology eddy kinetic energy and root-mean-square vertical velocity w_{rms} averaged over $200 \times 200 \text{ km}$ domain. (g) A conceptual diagram of the three-layer structure of the water column based on the change of dynamics.

still relatively high but decaying EKE and small w_{rms} , Quiescent layer ($>1,000 \text{ m}$) with weak and relatively steady flows (Figure 3g).

3.1.2. Statistics of the Source Regions

A source region of particles is taken as a particle cloud for statistical analysis. We adopt the general notions in LaCasce (2008) to quantify the variability of particle source regions. Three moments (mean, variance, and kurtosis) are derived from the probability density function (PDF) of the horizontal displacements for monthly backtracking of particles.

The mean describes the movement of the center of mass

$$M = \sqrt{M_x^2 + M_y^2} \quad (1)$$

with

$$M_x = \frac{1}{N} \sum_{i=1}^N [x_i - x_{i_0}], \quad (2)$$

$$M_y = \frac{1}{N} \sum_{i=1}^N [y_i - y_{i_0}], \quad (3)$$

where (x_i, y_i) gives the horizontal position of particle i when it reaches 200 m depth, and (x_{i_0}, y_{i_0}) is its initial position.

The horizontal displacement relative to the center of mass for a single particle is given by

$$r_i = \sqrt{[x_i - x_{i_0} - M_x]^2 + [y_i - y_{i_0} - M_y]^2}. \quad (4)$$

The variance measures how particles spread out, namely, the size of the particle cloud (also referred to as "cloud dispersion")

$$D = \frac{1}{N-1} \sum_{i=1}^N \left([x_i - x_{i_0} - M_x]^2 + [y_i - y_{i_0} - M_y]^2 \right) \\ = \frac{1}{N-1} \sum_{i=1}^N r_i^2. \quad (5)$$

The kurtosis is used to reflect the spatial distribution of particles

$$ku \equiv \frac{\sum_i r_i^4}{[\sum_i r_i^2]^2}. \quad (6)$$

A kurtosis close to 3 corresponds to a PDF following a nearly Gaussian distribution, which is the case for randomly moving particles. In contrast, particles advected by turbulent flows tend to distribute in tight clusters, characterized by a kurtosis higher than 3.

We choose particles sinking at 50 m d^{-1} backtracked from 1,000 m as an example for the following analyses. This choice is a good compromise between the realistic range of sinking velocity and the ability to reflect the influence of flow dynamics in the twilight zone. The 20 m d^{-1} sinking group is shown in the time series as well to indicate how slow-sinking particles are affected.

The center of mass mostly moves around the PAP site within a diameter of 100 km for particles sinking at 50 m d^{-1} and 200 km for the sinking group 20 m d^{-1} (Figure 4a), as shown by the source areas in Figure 2. The two sinking groups show similar variability in the monthly statistical funnel: local kurtosis peaks appear to arise with low mean and variance. Since the end of 2002, valleys of variance often occur with small means and large kurtosis, corresponding to a local source region with a center of mass adjacent to the PAP site. Kurtosis peaks larger than 3 indicate extended tails in the PDF of horizontal displacement, which means the distribution of particles is highly heterogeneous (Figure 4c).

The presence of mesoscale eddies is most likely responsible for shaping particle distributions. Three indicators depict local mesoscale activity within a $100 \times 100 \text{ km}$ area centered on the PAP site (Figures 4d–4f). Sea level anomaly (SLA) reveals eddy features at the surface, relative vorticity $\zeta = v_x - u_y$ and Okubo-Weiss parameter $OW = \sigma^2 - \zeta^2$ where the strain magnitude $\sigma = \sqrt{(u_x - v_y)^2 + (v_x + u_y)^2}$, indicate signatures of mesoscale eddies at 500 m. We highlight eight periods based on their dispersion metrics showing local peaks of kurtosis with low mean and variance, associated with distinct signals of mesoscale eddies (half anticyclones and half cyclones, marked by the blue/red vertical lines in Figure 4). A reference period, January 2006, is chosen to compare with the former periods. Note that the reference period is characterized by a higher variance, much lower kurtosis, and no signature of local mesoscale dynamics.

3.2. Horizontal Advection

3.2.1. Horizontal Dispersion in the 3D Field

Source distributions of particles collected at 1,000 m during two representative eddy-dominated periods and the reference period are shown in the top panel of Figure 5. Particle sources were highly concentrated around the PAP site during December 2002 and May 2007, in response to the local presence of mesoscale eddies (Figures 5d and 5f). In contrast, no particular hot-spot of particle source locations is seen embracing the PAP site in January 2006 when the vorticity does not dominate (Figure 5e). This situation is representative of conditions without a single-dominant eddy structure.

The measures in Figure 4 derived from the PDF of horizontal displacements have described the shape of statistical funnels as a result of particle dispersion. We adopt notions in Poje et al. (2010) to further describe the temporal evolution of horizontal dispersion by computing single-particle dispersion and pair dispersion (Figures 5g and 5h). The former, also termed absolute dispersion, describes the spreading of particles. Denoting the trajectory of a particle by $\mathbf{x}(\mathbf{a}, t)$ where the label $\mathbf{a} = \mathbf{x}(\mathbf{a}, t_0)$, the horizontal absolute dispersion A_h^2 is defined as the mean-squared horizontal displacement

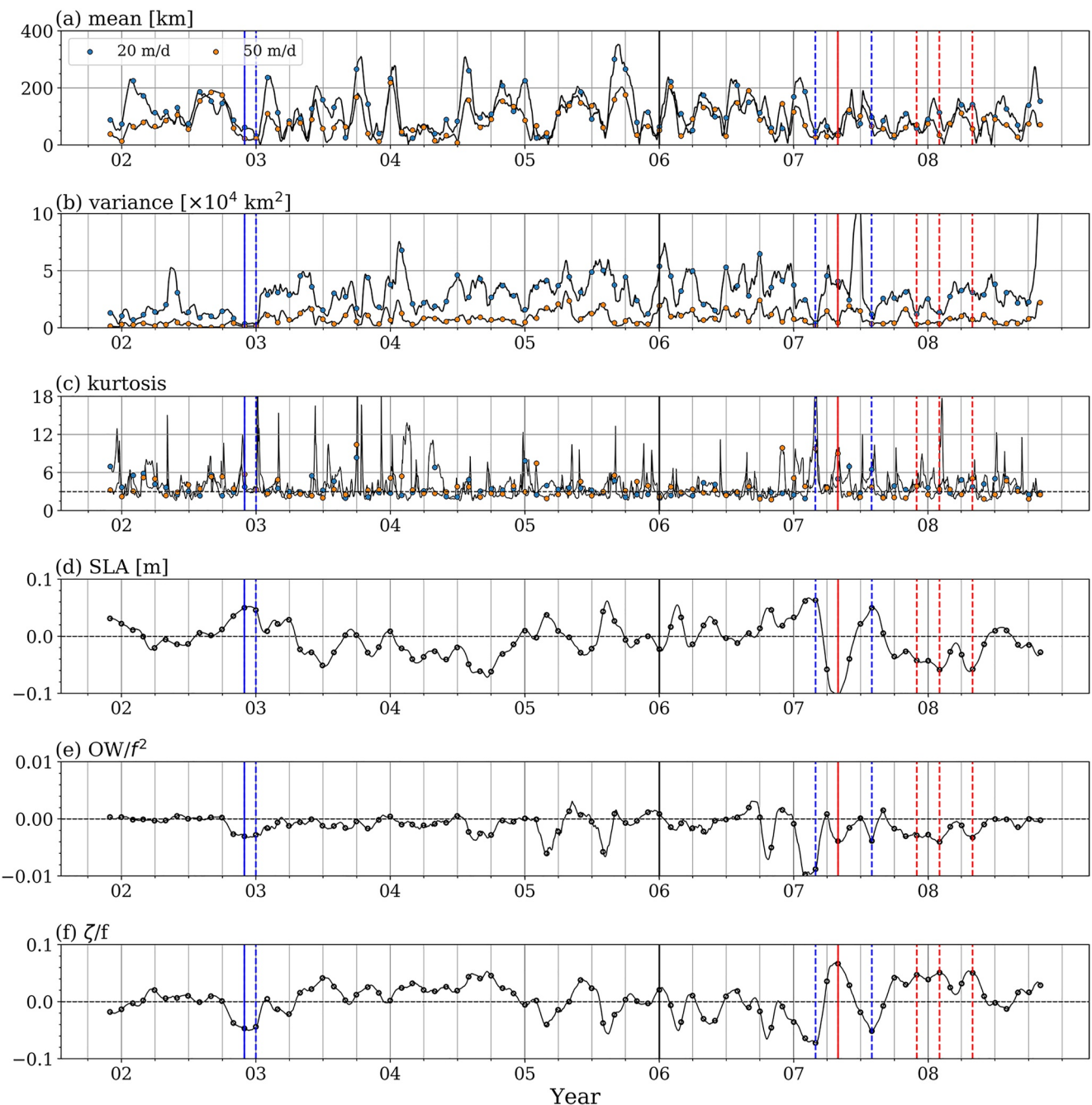


Figure 4. Time series of dispersion metrics derived from the probability density function (PDF) of particle horizontal displacements, for particles backtracked from 1,000 m sinking at 50 and 20 m d⁻¹: (a) mean; (b) variance; (c) kurtosis. (d–f) Monthly averaged sea level anomaly (SLA), Okubo-Weiss parameter normalized by f^2 and relative vorticity normalized by f in a 100 × 100 km square centered on Porcupine Abyssal Plain site. The vertical lines mark the typical months selected for further analysis: blue for the anticyclonic eddy dominated period, red for the cyclonic eddy dominated period, and black for the reference period (non-vorticity-dominated case). Solid lines highlight the main examples used in detailed analyses in Section 3.2, while the dashed lines mark alternative cases to firm the results presented in Section 3.4. The x -axes are labeled with “year” at the beginning of each year.

$$A_h^2(t) = \langle (\mathbf{x}_h(\mathbf{a}, t) - \mathbf{a}_h)^2 \rangle \quad (7)$$

where $\langle \rangle$ denotes the ensemble average. The horizontal relative dispersion D_h^2 measures particle pair dispersion that depicts the stirring process. That is, the mean-squared horizontal separation of particle pairs initially defined at the beginning of particle release. The relative separation of a particle pair ($\mathbf{a}_1, \mathbf{a}_2$) is computed as

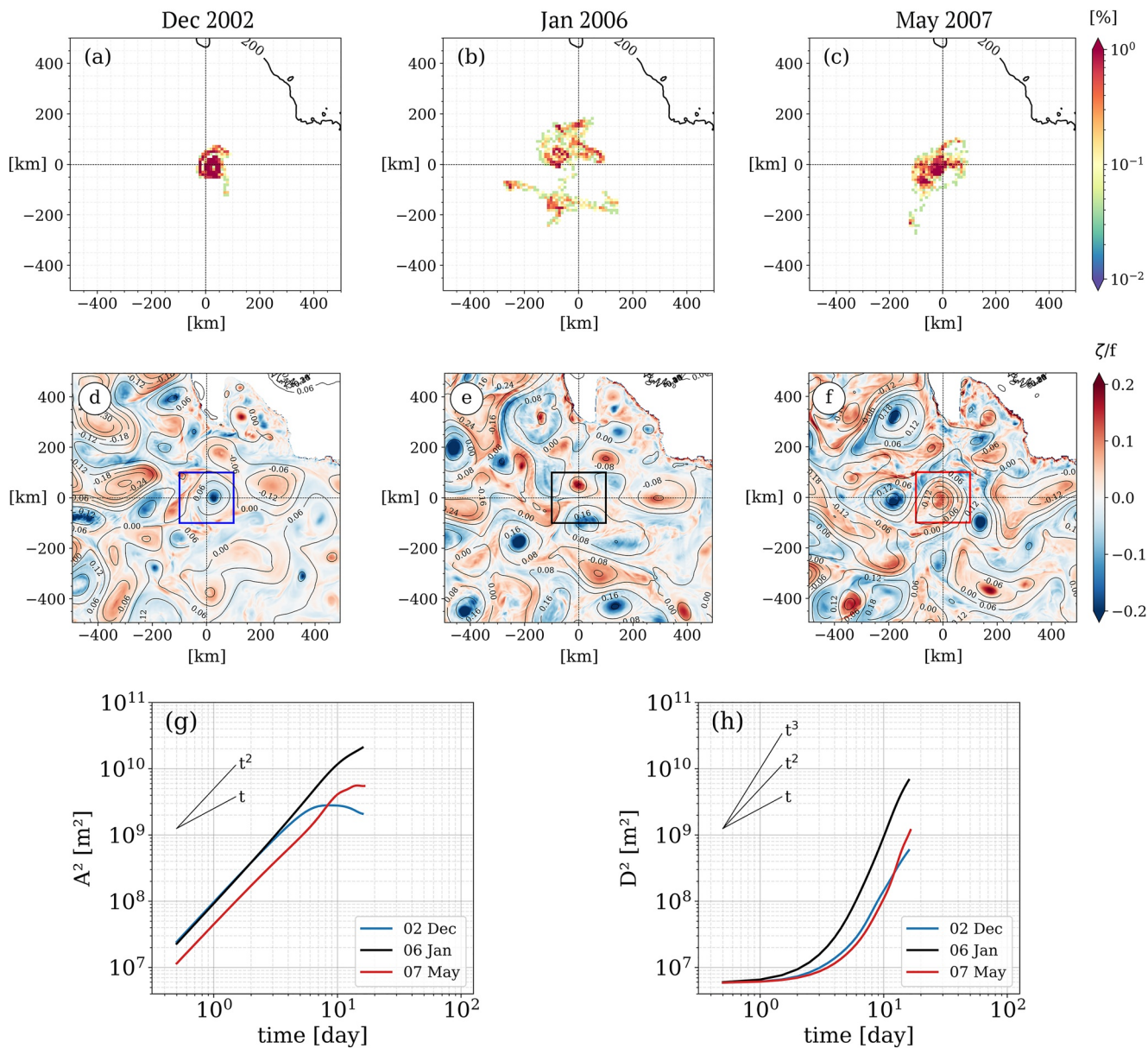


Figure 5. (a–c) Probability density of particles sinking at 50 m d⁻¹ to the 1,000 m trap during three example periods. (d–f) Monthly averages of relative vorticity at 500 m with contours of sea level anomaly. (g–h) The group averaged absolute and relative dispersion. The “time” on the x-axis represents days after particles are released, that is, particle “age”.

$$\mathbf{D}(t, \mathbf{D}_0) = \mathbf{D}_0 + (\mathbf{x}(\mathbf{a}_1, t) - \mathbf{x}(\mathbf{a}_2, t)) \quad (8)$$

with the initial distance between the two particles in a pair $\mathbf{D}_0 = \mathbf{a}_1 - \mathbf{a}_2$. Here we consider the horizontal separation only:

$$D_h^2(t) = \langle \mathbf{D}_h(t) \cdot \mathbf{D}_h(t) \rangle \quad (9)$$

The horizontal absolute dispersion A_h^2 first follows a ballistic regime $A_h^2(t) \propto t^2$ at small time scales of several days. The non-locality indicates the dominance of mesoscale dynamics in absolute dispersion. At intermediate time scales, an anomalous dispersion regime occurs with $A_h^2(t) \propto t^\alpha$ where α varies between 1 and 2. A diffusive regime $A_h^2(t) \propto t$ characterized by a slope close to 1 is expected after a long time when the absolute dispersion linearly grows in time. However, the large spatio-temporal inhomogeneities in mesoscale ocean flow

often prevent the presence of such a regime. The slopes for December 2002 and May 2007 ultimately fall below 1 as most particles stay trapped within an eddy and cannot spread further.

Relative dispersion depicts smaller-scale motions affecting relative diffusivity. It shows less difference in slopes. The horizontal relative dispersion D_h^2 first shows an exponential growth within approximately 5 days, typically occurring at spatial scales smaller than the deformation radius (10–20 km). In the next stage, D_h^2 follows a regime $D^2(t) \propto t^\beta$ with $2 < \beta < 3$ related to motions at local scales. The evolution of absolute and relative dispersion suggests reduced particle spread when a strong eddy persists around the PAP site.

3.2.2. Dynamical Regimes of Horizontal Dispersion

Horizontal dispersion in the 3D field is also affected by vertical dispersion. Particles of the same age can vertically separate by a few hundred meters when backtracked into the upper ocean. Particles may thus experience different dynamical regimes over a range of depths and may also be affected by a vertical shear (Berti & Lapeyre, 2021). Results of 2D experiments illustrate different dynamical regimes from 200 down to 4,000 m. The visual appearance of particle trajectories suggests the dominance of mesoscale activity in transporting and trapping particles (Figures 6a–6c). Comparisons between trajectories at different depths identify that the transition depths for dynamical regimes are 500 and 1,000 m, consistent with the three-layer structure of the water column in Figure 3. In the energetic regime of horizontal advection above 500 m, particles from 200 km away or further can also reach the site in the reference case (January 2006). At the base of the twilight zone (1,000 m), the regime switches from the upper ocean with active eddies to the quiescent deep ocean. The clusters of dispersion curve for the upper ocean, middle, and deeper depths verify the regimes categorized by 2D trajectories. At intermediate stage (about 5 days), the power-law regime $D^2(t) \propto t^\beta$ with $2 < \beta < 3$ is only seen at depths above 1,000 m. It underlines the existence of small-scale motions in the upper two layers. Similar to 3D experiments, the flattening dispersion curves starting from about 5 days after the release for December 2002 and May 2007 illustrate lower dispersion of particles in the twilight zone, mostly confined within the 200×200 km box.

3.3. Vertical Advection

To evaluate the impact of vertical advection, we examine the time taken by particles to sink from the export depth to the trap depth, termed as “travel time.” The influence of vertical flow on particle sinking can be reflected by the travel time anomaly Δt , which is the difference between the travel time t and the standard sinking time t_0 without the presence of ocean vertical flows. The amplitude of the monthly mean Δt for particles backtracked from 1,000 m can reach up to 7% (~ 1 day) of the expected travel time for 50 m d^{-1} particles and 12% (~ 5 days) for 20 m d^{-1} (Figures 7a and 7b). For individual particles, the maximal amplitude can reach up to 5 days for 50 m d^{-1} particles and 20 days for 20 m d^{-1} . Such time lags are significant for POC measurements during bloom/post-bloom periods when the production rapidly varies over days. On average, the negative $\Delta t/t_0$ in most of the experiments indicates that particles take less time to reach the trap due to the acceleration by downward ocean vertical velocity. There is no distinct seasonality found in mean Δt . However, the variance $V(\Delta t)$ commonly peaks in spring, in agreement with large vertical velocities between 200 and 400 m during this period (Figures 3e and 3f). The standard deviation reaches up to 2 days for 50 m d^{-1} particles and 6 days for 20 m d^{-1} . In Figure 7c, the distribution of seasonal and full-period Δt for particles sinking at 50 m d^{-1} shows a broader PDF in spring, in line with the seasonal variability of $V(\Delta t)$. The PDF of travel time t for the full period also displays slight asymmetry toward shorter time, and the asymmetry is more distinct for smaller sinking velocities and deeper trap depth (Figures 7d and 7e). Liu et al. (2018) found that the vertical advection in the upper 200 m largely intensifies particle export with sinking speeds from 20 to 100 m d^{-1} . Our results additionally show that the vertical advection below 200 m also enhances the export of particles.

3.4. Linking the Particle Export With Specific Features

Following the work of Balwada et al. (2021), we use the joint probability distribution function (JPDF) of vorticity and strain to decompose the flow field into regions with different dynamical features. The term “vorticity” refers to the vertical component of vorticity normalized by the Coriolis frequency ζ/f , where $\zeta = v_x - u_y$. The “strain” is the strain magnitude normalized by the Coriolis frequency σ/f , where $\sigma = \sqrt{(u_x - v_y)^2 + (v_x + u_y)^2}$. The JPDF

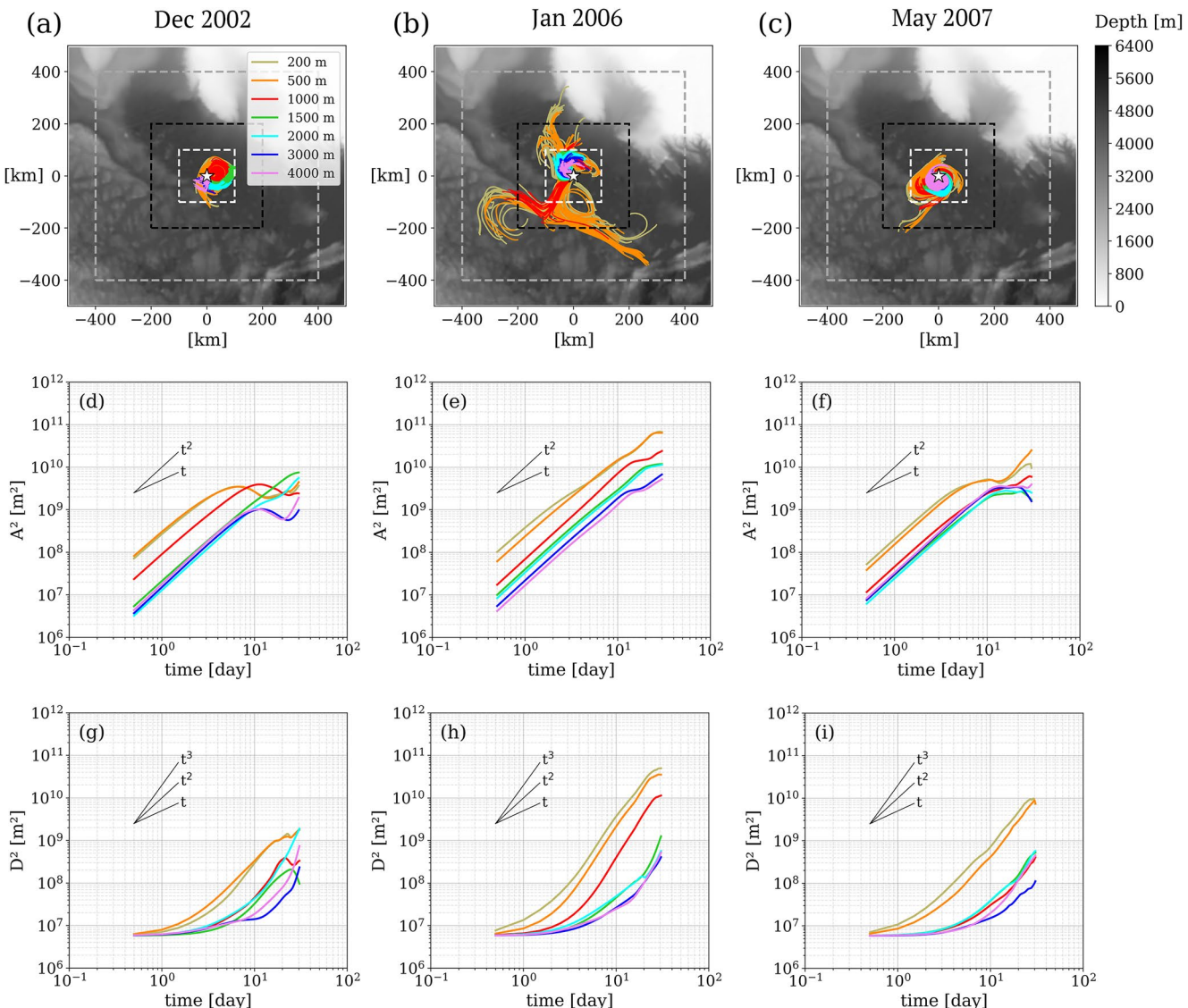


Figure 6. Trajectories and dispersion of particles in 2D simulations during the three example periods. (a–c) Trajectories of 200 particles randomly selected from 2,160 particles backtracked at each depth in a month. The white star in the center represents the Porcupine Abyssal Plain site. The small white square (200×200 km) highlights the region with particles concentrated at all depths. The medium black square (400×400 km) covers most particle trajectories backtracked below 1,000 m. The large gray square (800×800 km) contains all particle trajectories. The middle and bottom rows are (d–f) absolute dispersion and (g–i) relative dispersion as a function of release time.

identifies three regions in the flow field separated by the lines of $\sigma = |\zeta|$: anticyclonic vorticity dominated (AVD) region where $\zeta < 0$ and $\sigma < |\zeta|$; cyclonic vorticity dominated (CVD) region where $\zeta > 0$ and $\sigma < |\zeta|$; and strain dominated (SD) region where $\sigma > |\zeta|$. Figure 8 shows the JPDF of full-period Lagrangian data and Eulerian field for the two layers of the twilight zone (200–500 and 500–1,000 m). The Lagrangian JPDF on the top row of Figure 8 displays no distinct skewness. Hence, particles do not show a specific preference in sampling different flow structures over the long term.

Vertical velocity patterns are qualitatively similar between the Eulerian and Lagrangian diagnostics. At all depths, the AVD region is featured with downwelling, whereas the CVD region is dominated by upwelling, in accord with the picture of the vertical velocity below the mixed layer in Balwada et al. (2021). In the SD region, vertical velocity patterns change with depth. Below 500 m, vertical velocities are negative close to the line $\sigma = \zeta$, corresponding to the cyclonic side of fronts, and positive on the anticyclonic side (Figure 8h). Such a pattern

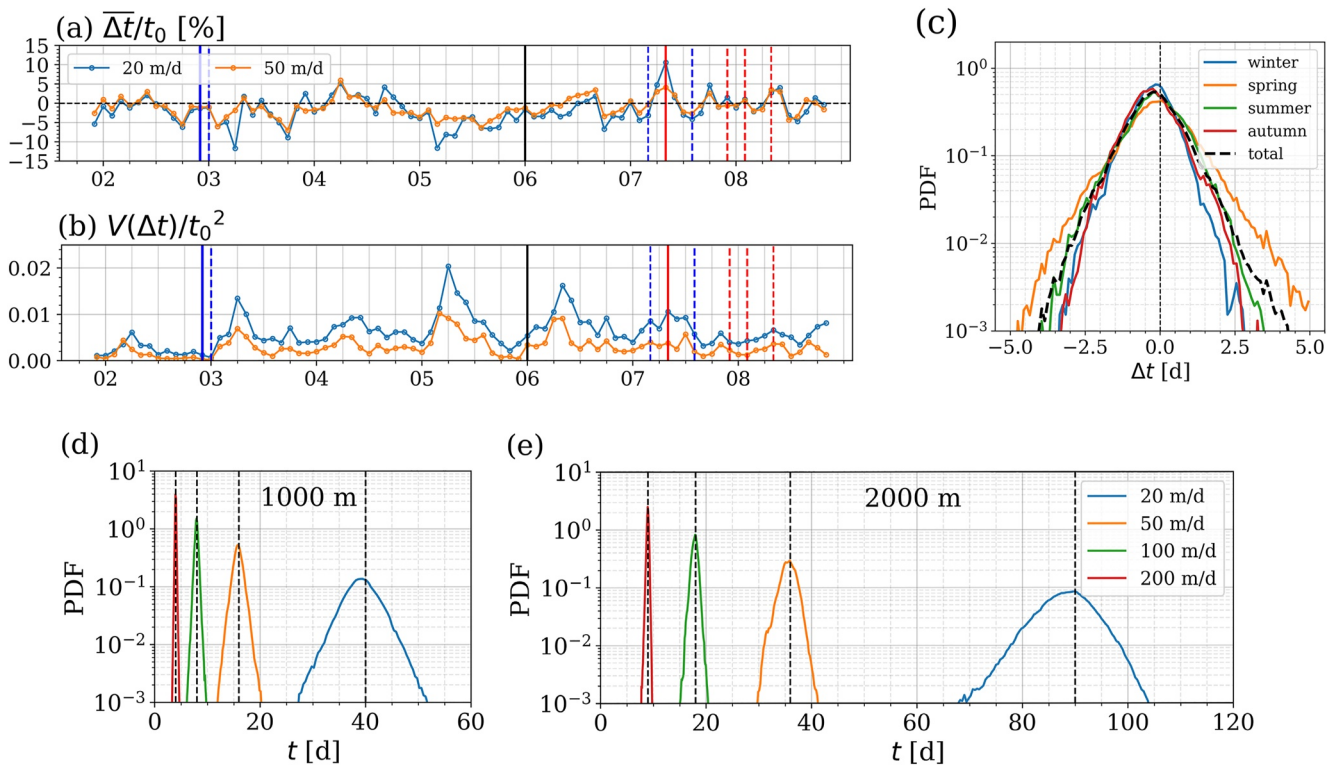


Figure 7. Metrics of vertical dispersion for particles backtracked from 1,000 m sinking at 50 and 20 m d⁻¹: (a) The percentage of mean travel time anomaly ($\bar{\Delta}t$) to the standard travel time t_0 ; (b) Variance of Δt normalized by t_0^2 . The colored vertical lines are the same as those in Figure 4, which marks months with local coherent anticyclonic eddy (in blue), cyclonic eddy (in red), and a reference case without coherent structure at the site (in black). (c) Probability density function (PDF) of the travel time anomaly Δt for particles sinking at 50 m d⁻¹ backtracked from 1,000 m depth, over full-period (7 years) and different seasons. (d and e) The PDF of travel time t over the 7-year full period for four sinking velocities and two trap depths.

is expected from frontal dynamics, and again in accord with results shown in Balwada et al. (2021) below the mixed-layer. However, between 200 and 500 m, only upwelling is visible in the SD region on both sides, apparently contradicting classical expectations.

An important difference in our computation is that the vorticity and strain are computed at the same depth as the vertical velocity, which is different from the vorticity-strain space defined at the surface only in Balwada et al. (2021). Comparisons between the w patterns depending on the depth chosen to compute vorticity and strain are shown in Figure S3 in Supporting Information S1. If the vorticity and strain are computed at the surface, we recover the expected signs for vertical velocity: downwelling on the cyclonic side and upwelling on the other side at all depths (100 m, 200 m, 500 m). However, when the vorticity and strain are computed at the corresponding depth of vertical velocity, the patterns are reversed at 200 and 500 m. This can be attributed to the presence of numerous frontal structures with an inversion of sign for relative vorticity in the vertical, while the sign of vertical velocity remains vertically homogeneous (Figure S4 in Supporting Information S1). This is a robust feature in our simulation for all times and locations, and it will be addressed further in future research.

Patterns of particles and their associated vertical velocities are shown more specifically for cases corresponding to the presence of anticyclonic or cyclonic eddies in Figure 9. On the top row, the composite distribution of particles on the vorticity-strain space for months with coherent anticyclonic eddies shows a high density of particles along the $\sigma = -\zeta$ line, with a preference in the SD region (Figure 9a). These particles are likely located in the filamentary vorticity streaks along with the swirl, which highlights the footprints of particles on the periphery of the eddy. Vertical velocities recorded by particles in Figure 9b also show upward velocities despite the dominance of downward velocities, consistent with the full-period pattern in Figures 8b and 8d. From the PDF of travel time anomaly Δt , we find that the upward velocities are mostly associated with March 2007, which has a longer tail toward positive Δt and slight skewness. It differs from the other 3 months in winter and summer with apparently

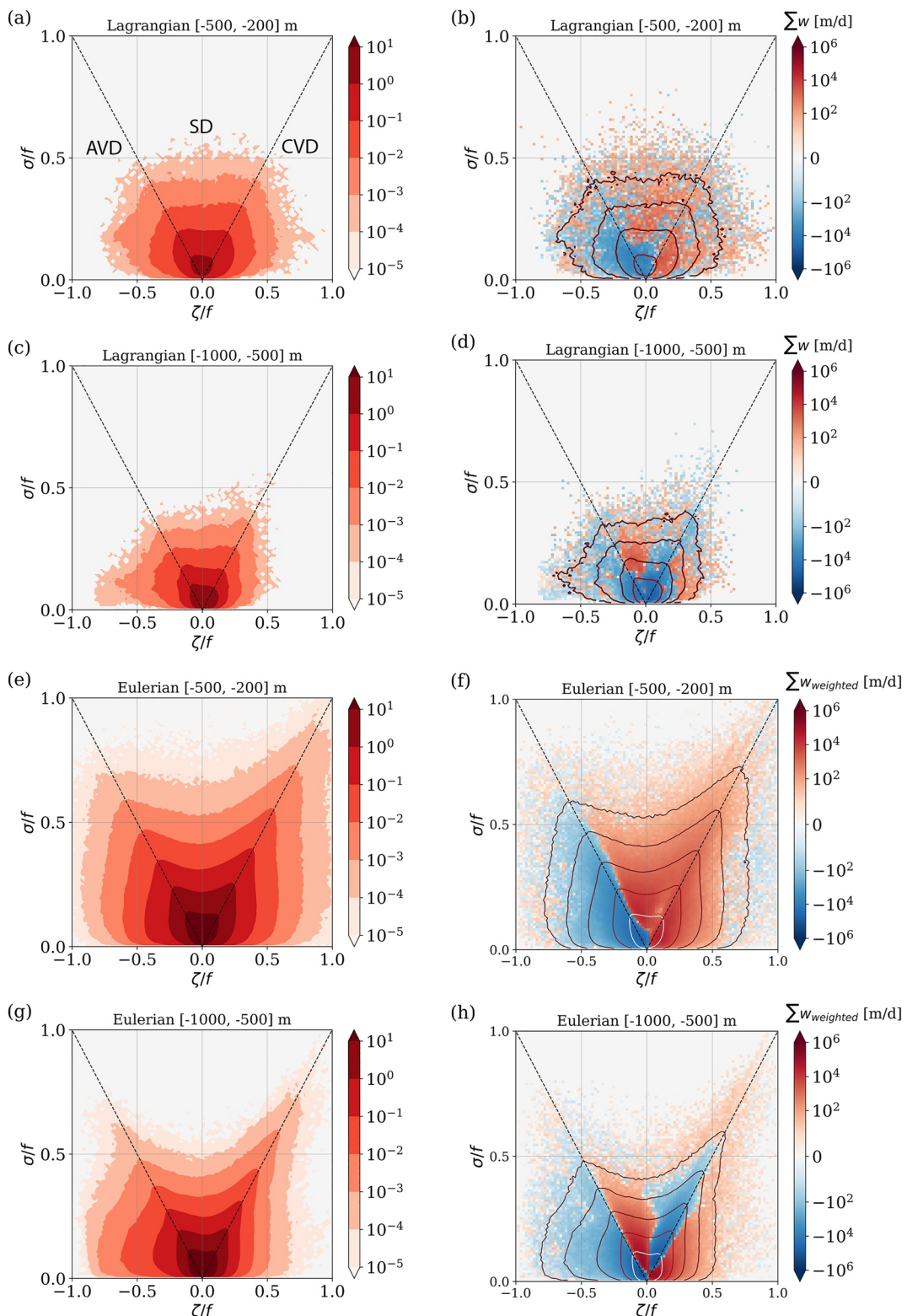


Figure 8. Comparison of Lagrangian trajectories (sinking velocity 50 m d^{-1}) and Eulerian field (domain size: $200 \times 200 \text{ km}$) on the vorticity-strain space. Left column: Joint Probability Density Function (JPDF). The x - y space is divided into three regions: anticyclonic vorticity dominated (AVD), cyclonic vorticity dominated (CVD), and strain dominated (SD). Right column: vertical velocity w conditioned on the vorticity-strain space, shown as the sum of w in each bin, contoured by the particle density. The sum of Eulerian w is weighted by the thickness of each depth layer in the sigma coordinate. (a and b) For particle footprints in 200–500 m. (c and d) For particle footprints in 500–1,000 m. (e and f) For the Eulerian field in 200–500 m. (g and h) For the Eulerian field in 500–1,000 m.

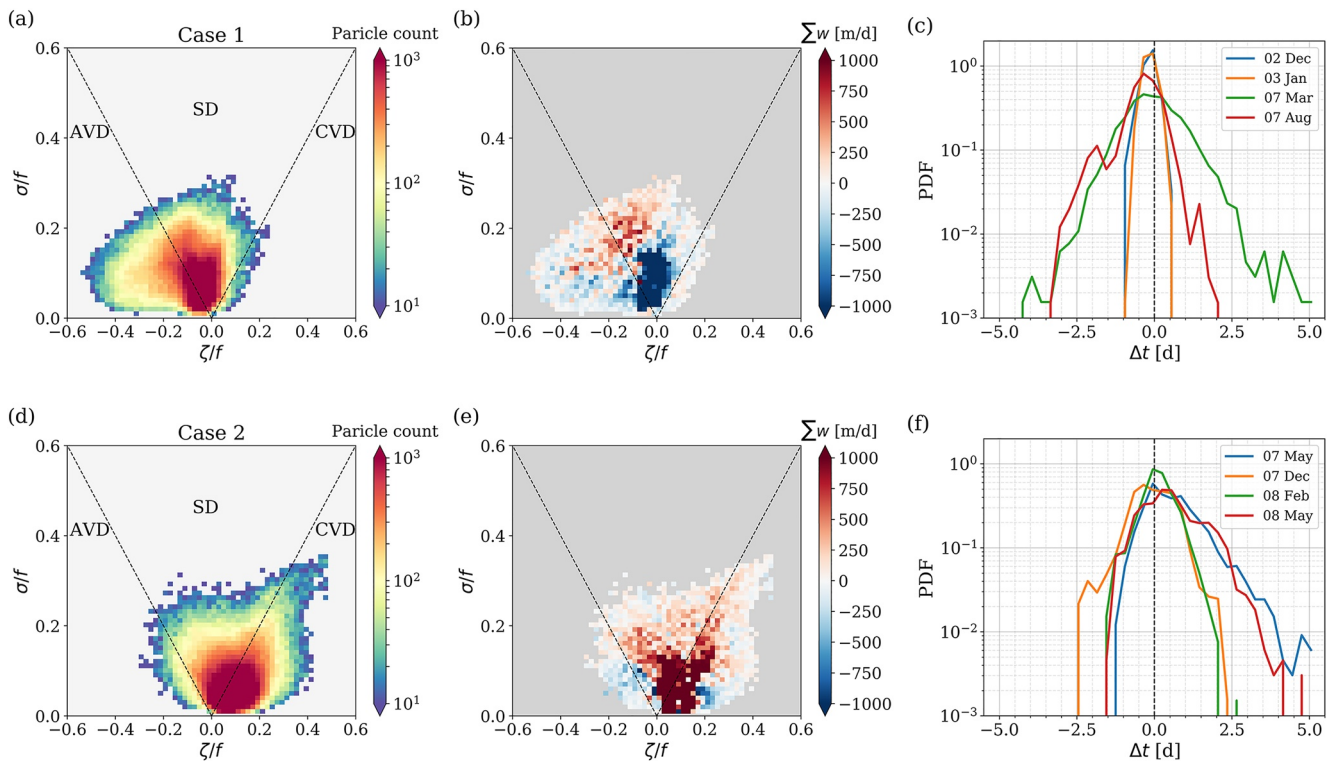


Figure 9. Composite plots of the eddy dominated periods: (a–c) Case 1: anticyclonic eddy-dominated periods; (d–f) Case 2: cyclonic eddy-dominated periods. From left to right columns are particle count on the vorticity-strain space, the conditioned sum w , and PDF of travel time anomaly Δt .

skewed PDF toward negative Δt , as more energetic eddies in spring allow particles to sample complex flow structures. Therefore, even the same type of mesoscale features can exert different impacts on the vertical dispersion of particles. Unlike the strain-dominated pattern in the anticyclone case, particle trajectories in cyclonic eddies concentrate in the CVD region with only a smaller portion in the SD part (Figure 9d). The cyclonic vortex is responsible for the majority of upward velocities recorded by particles, leading to a PDF of Δt significantly extended to the positive side, especially in spring months.

Overall, JPDFs show major trends here: at monthly time scales, anticyclonic eddies accelerate the downward transport while cyclonic eddies delay the descent of particles. However, the patchy vertical velocity patterns in mesoscale eddies are more complicated than the classic eddy-pumping mechanism that upwelling is always in cyclonic eddies and downwelling is always in anticyclonic eddies. This mechanism is more applicable in the period of formation and strengthening of eddies, whereas the case of eddy decay shows opposite patterns (Klein & Lapeyre, 2009). Furthermore, the vertical velocity patterns in eddies are not in general uniform. Instead, a set of upward and downward cells are formed extending from the center to the perimeter (Pilo et al., 2018). Besides, many other mechanisms including eddy propagation (McGillicuddy et al., 1995), eddy-eddy interactions (Pidcock et al., 2013) and submesoscale processes (Brannigan, 2016) may also contribute to the vertical velocity structure within the eddy. The complexity of mechanisms implies that a detailed analysis of individual eddies (e.g., eddy age and status, particle location) is required to link particle export with specific features.

4. Discussion and Conclusions

In this study, we backtracked virtual particles from locations of deep-moored sediment traps to the export depth using a realistic eddy-resolving simulation. We applied a set of dispersion metrics to characterize particle trajectories and link them with mesoscale dynamical features. Here we summarize the main conclusions and discuss the simplifications in our work and implications for future study.

4.1. On the Simplifications

4.1.1. Export Depth

We found that mesoscale dynamics in the twilight zone (200–1,000 m) play a dominant role in shaping the statistical funnels based on several simplifications. We choose the base of the epipelagic layer (200 m) as the end depth of particle backtracking. The reason is that we are focusing on the fate of particles once they are formed and exported below the productive surface layer. However, the uniform end depth in our study is not precisely an export depth. The export depth, in reality, varies with time and space and differs for particles with different sinking velocities.

4.1.2. Particle Sinking Velocity

Another simplification is that we use constant sinking velocities ranging between 20 and 200 m d⁻¹. Most of our choices fall into the common range of sinking velocities from 50 to 200 m d⁻¹ adopted in previous studies (Siegel & Deuser, 1997; Siegel et al., 2008; Waniek et al., 2000). It is noteworthy that 20 m d⁻¹ has also been used in a few recent studies of sediment trap catchment area (Liu et al., 2018; Wekerle et al., 2018). However, particle sinking velocity is highly likely to vary with depth. Remineralization leads to a decrease in the size of particles and possibly in their sinking velocity. Dever et al. (2021) suggests remineralization processes promote the contribution of slow-sinking particles (0.025–5 m day⁻¹) to the POC export. For the fast-sinking particles in our study, we assume the impact of remineralization is modest due to the short travel time. This consideration is supported by observations at the PAP site that demonstrate that fast-sinking particles were sufficient to supply deep POC flux. In contrast, slow-sinking particles were likely to be entirely remineralized in the twilight zone (Riley et al., 2012).

Furthermore, processes including aggregation, fragmentation, and zooplankton grazing also change particle size, density, and hence sinking velocity during particle descent (Boyd & Trull, 2007; Guidi et al., 2007; Riley et al., 2012; Trull et al., 2008). Considering the sinking velocity varying with depth, the statistical funnel of particles reaching the trap will be a mixture of source regions for a wide range of sinking classes. Nevertheless, this study deals with the impact of mesoscale dynamics on the dispersion and travel time of particles assumed to be conservative in the mesopelagic layer. Future research is required to include processes behind the changes in particle size and sinking rate (which are beyond the scope of this study).

4.1.3. The Heterogeneity of Particle Sources

This study analyzes statistical funnels sampled by deep sediment traps without considering the heterogeneity of particle sources. We identify the distribution of potential particle sources but do not address the temporal and spatial variability of carbon fluxes at depth. Both satellite observations (Zhang et al., 2019) and modeling investigations (Lévy et al., 2014) have shown undoubtedly that the dynamics at medium and small scales strongly control the intensity of the primary production. The intensity of primary production largely constrains particle size spectra: higher production is generally associated with larger sizes (Kostadinov et al., 2009). Although simple relationships between particle size and sinking velocity are not straightforward (Iversen & Lampitt, 2020), to a first approximation, these two parameters can be related by Stokes' law (Lerman et al., 1974; Laurenceau-Cornec et al., 2020). Therefore, the next step will be to examine the impact of sinking velocity variability by weighting the particle size distribution correlated with the PP intensity at the time and location of particle formation. The primary production distributions could be estimated by coupling the dynamic model with a simple NPZD model. From a model perspective, this exercise will give us the first information on the eddy-scale variability of carbon fluxes in the deep ocean with a daily resolution. Also, it will allow a first analysis of the (de)coupling between export production below the mixed layer and deep fluxes at mesoscales (with nevertheless, the conservation of particles as a strong hypothesis at the first stage). In addition, by using "realistic" simulations from operational models, these backward simulations can provide relevant information about sources and time lags of particles collected in sediment traps during process study cruises.

4.2. Implications for Studying the POC Flux

4.2.1. Submesoscale Motions Below the Mixed Layer

From a physical perspective, the end depth of 200 m is close to the typical deep winter mixed layer depth in our study region. As such, submesoscale processes, which are more intense within the winter mixed layer, appear to

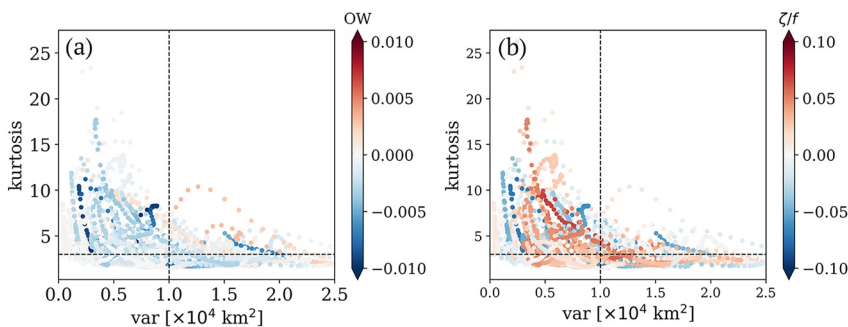


Figure 10. Relation between kurtosis and variance from 30-day moving average time series for 50 m d^{-1} , trap $1,000 \text{ m}$, colored by (a) Okubo-Weiss parameter and (b) relative vorticity. The dashed lines mark variance $= 1 \times 10^4 \text{ km}^2$ and kurtosis $= 3$.

play a minor role in particle transport below 200 m. Previous studies have found that submesoscale dynamics can enhance particle export through advecting slow-sinking particles (Dever et al., 2021) or restratifying the mixed layer to reduce the impact of vertical mixing on gravitational settling (Taylor et al., 2020). The rapid accumulation of particles has also been observed in the surface convergence zones associated with large vertical velocities (D'Asaro et al., 2018; Poje et al., 2014), such areas also have the potential to be hot spots of particle export to the deep ocean. However, how much submesoscale motions come into play below the mixed layer remains unclear.

Although highlighting the importance of mesoscale dynamics, this study points to an emergence of submesoscale motions below the mixed layer. There is a skewness in the vorticity-strain JPDF of the Eulerian field, extending along $\sigma = \zeta$ toward the cyclonic side of the frontal region. In addition, the asymmetry in the travel time anomaly reflects a skewed distribution of w toward downward velocity. The two findings unveil the manifestation of submesoscale motions characterized by positive skewness of relative vorticity (Buckingham et al., 2016; Rudnick, 2001) and an enhancement of downwelling (Dever et al., 2021; Thomas et al., 2008). Thus, higher resolution modeling is in demand to disentangle the impact of smaller scales in the mesopelagic layer, which may not be negligible. Yet we should keep in mind that the influence of submesoscale motions to export in this region is limited due to the constricted overlap of strong submesoscale instabilities in winter and large particle export in spring and summer (Erickson & Thompson, 2018).

4.2.2. The Sampling Design of a Regional Survey

This study underlines the impact of mesoscale dynamics in the twilight zone on the 3D transport of particles at a temperate open-ocean site. The presence of coherent mesoscale eddies can effectively “trap” particles within a local area ($<100 \text{ km}$) over a monthly time scale. Given the smaller statistical funnel confined by eddies, the export flux measured by the deep-ocean sediment traps is easier to be correlated to the surface production when a coherent structure persists right above the trap. This finding has implications for the sampling design in a regional survey, for example, the cruise scheduled in 2023 for the APERO project. As is often done during field surveys, the location of process study stations can be identified by focusing on these coherent mesoscale patterns, highlighted by satellite observations and modeling outputs. However, these structures only cover about 20% of the ocean, and particles are not always completely moving with these eddies. The eight eddy-dominated months in our analysis are based on the PDF of horizontal particle displacements. In general, high kurtosis correspond to low variance, associated with a negative Okubo-Weiss parameter and high relative vorticity (Figure 10). It indicates that coherent structures lead to hot spots of particle sources. Nevertheless, the continuum between coherent structures and turbulent flows (high variance, small kurtosis close to 3) represents a large portion of the ocean and should also be sampled. Thus sampling the remaining more turbulent and chaotic ocean is fundamental and challenging.

4.2.3. Generalization to Other Regions

While we expect our results to qualitatively hold in other regions of the ocean, the size of the statistical funnel and amplitude of the travel time anomalies will be a function of the local hydrodynamical properties, in particular of the mesoscale turbulence. A first attempt to generalize our results can be made by casting them in terms of non-dimensional parameters. We use the containment radii ($R_{95\%}$) and normalized root-mean-square travel time

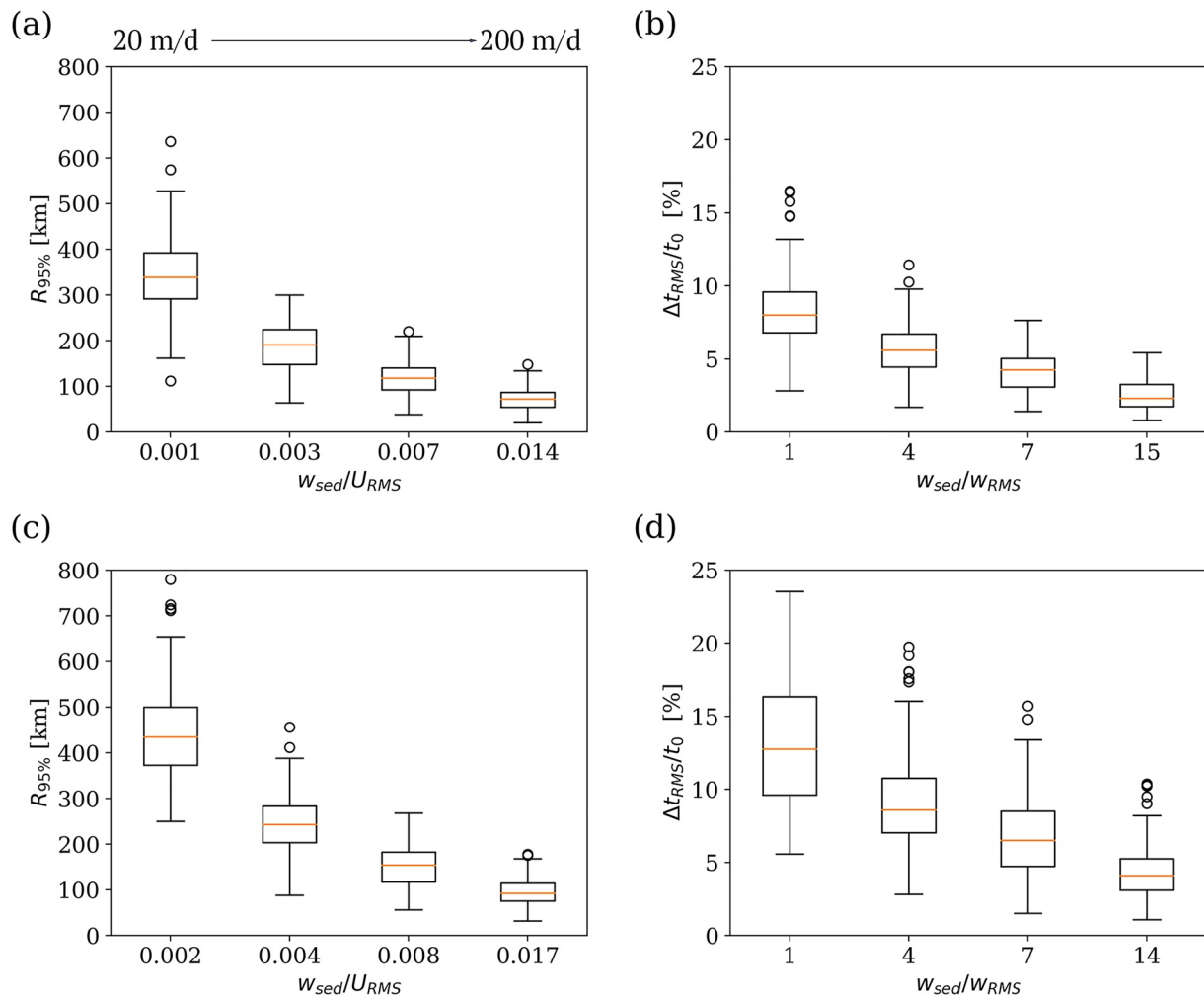


Figure 11. Full-period monthly horizontal and vertical dispersion metrics as a function of the ratio of sinking speed (from left to right: 20, 50, 100, 200 m day⁻¹) to the flow velocity. Top panel for particles backtracked from 1,000 m: (a) The radial distance containing 95% of the source region ($R_{95\%}$), corresponding to the ratio of particle sinking velocity (w_{sed}) to the root-mean-squared (RMS) horizontal current velocity (U_{RMS}). (b) RMS travel time anomaly (Δt_{RMS}) normalized by standard travel time t_0 , corresponding to the ratio of particle sinking velocity to the RMS vertical flow velocity (w_{RMS}). Bottom panel (c and d): same as a and b, for particles backtracked from 2,000 m.

anomaly ($\Delta t_{RMS}/t_0$) to describe horizontal and vertical dispersion of particles, respectively, and relate them with the ratio of particle sinking velocity to the flow velocity (Figure 11). The size of particle source regions for the trap at 1,000 m has $R_{95\%}$ mainly in the range of 300–400 km for w_{sed}/U_{RMS} at 0.001. It decreases by half when w_{sed}/U_{RMS} increases to 0.003. For a much higher speed ratio like 0.007 and 0.014, the containment radii remain at around 100 km or less. The vertical dispersion is most significant when w_{sed}/w_{RMS} is 1, with the percentage of travel time anomaly close to 15% (~5 days). The deviation matters for the short-term deployment of sediment traps during the bloom/post-bloom period. Note that the relationship between dispersion metrics and speed ratio depends on the trap depth. For the trap at 2,000 m, the source region expands only by a few tens of kilometers compared to 1,000 m. The travel time anomaly increases more obviously. The 75th percentile for 20 m day⁻¹ is more than 15%, which is equivalent to 15 days. Even for 50 m day⁻¹, it is around 10% (4 days). If such relationships hold for other dynamical regimes, these numbers could be a reference for estimating the source region and time lags of particle sinking, given by the current velocity data at other locations.

Moreover, we proposed a three-layer structure of dynamical regimes, as reflected by flow properties and horizontal dispersion in 2D experiments. In particular, the PAP site is characterized by a moderate mesoscale activity compared to other regions like the Gulf of Mexico (Liu et al., 2018) and the Arctic Ocean (Wekerle et al., 2018). The vertical structuring of particle dispersion associated with small-scale dynamics (200–500 m: high EKE and

w , 500–1,000 m: still relatively high EKE, but small w ; below 1,000 m: quiet, smooth flows) must be confronted with different situations. It is necessary to verify the generalization of this finding in other regions. Future work could be first at a regional scale to check the homogeneity of dispersion statistics in the inter gyre region of the North Atlantic, near the PAP station. Second, a similar analysis could be conducted at other long-term observatory stations (e.g., BATS, HOT) and in situ experiments in Eastern Boundary Upwelling Systems, where many dedicated cruises have been conducted. Lastly, different turbulent and dynamical regimes such as Western Boundary Currents and the Southern Ocean, where the correlation between strong turbulent regimes and horizontal velocities remains a big issue, are also hotspots worth studying.

Data Availability Statement

Coastal and Regional Ocean COMmunity ocean model is available at <https://www.croc-ocean.org>. The Lagrangian particle tracking software Pyicles is available at <https://github.com/Mesharou/Pyicles> and has been published on Zenodo at <https://doi.org/10.5281/zenodo.4973786>.

Acknowledgments

This work was supported by the ISblue project, an Interdisciplinary graduate school for the blue planet (ANR-17-EURE-0015), and co-funded by a grant from the French government under the program "Investissements d'Avenir." This manuscript contributes to the APERO project funded by the National Research Agency under the grant APERO [Grant No. ANR-21-CE01-0027] and by the French LEFE-Cyber program. Simulations were performed using HPC resources from GENCI-TGCC (grant 2018-A0050107638) and from DATARMOR of "Pôle de Calcul Intensif pour la Mer" at Ifremer, Brest, France. The authors thank Mathieu Le Corre for providing CROCO simulation outputs. The authors appreciate the reviewers for their constructive comments and insightful suggestions that significantly helped improve this manuscript.

References

- Armstrong, R., Lee, C., Hedges, J., Honjo, S., & Wakeham, S. (2001). A new, mechanistic model for organic carbon fluxes in the ocean based on the quantitative association of POC with ballast minerals. *Deep Sea Research Part II: Topical Studies in Oceanography*, 49(1–3), 219–236. [https://doi.org/10.1016/s0967-0645\(01\)00101-1](https://doi.org/10.1016/s0967-0645(01)00101-1)
- Asper, V., Deuser, W., Knauer, G., & Lohrenz, S. (1992). Rapid coupling of sinking particle fluxes between surface and deep ocean waters. *Nature*, 357(6380), 670–672. <https://doi.org/10.1038/357670a0>
- Balwada, D., Xiao, Q., Smith, S., Abernathey, R., & Gray, A. (2021). Vertical fluxes conditioned on vorticity and strain reveal submesoscale ventilation. *Journal of Physical Oceanography*, 51(9), 2883–2901. <https://doi.org/10.1175/jpo-d-21-0016.1>
- Berti, S., & Lapeyre, G. (2021). Lagrangian pair dispersion in upper-ocean turbulence in the presence of mixed-layer instabilities. *Physics of Fluids*, 33(3), 036603. <https://doi.org/10.1063/5.0041036>
- Boyd, P., Claustre, H., Levy, M., Siegel, D., & Weber, T. (2019). Multi-faceted particle pumps drive carbon sequestration in the ocean. *Nature*, 568(7752), 327–335. <https://doi.org/10.1038/s41586-019-1098-2>
- Boyd, P., & Trull, T. (2007). Understanding the export of biogenic particles in oceanic waters: Is there consensus? *Progress in Oceanography*, 72(4), 276–312. <https://doi.org/10.1016/j.pocean.2006.10.007>
- Brannigan, L. (2016). Intense submesoscale upwelling in anticyclonic eddies. *Geophysical Research Letters*, 43(7), 3360–3369. <https://doi.org/10.1002/2016gl067926>
- Buckingham, C., Naveira Garabato, A., Thompson, A., Brannigan, L., Lazar, A., Marshall, D., et al. (2016). Seasonality of submesoscale flows in the ocean surface boundary layer. *Geophysical Research Letters*, 43(5), 2118–2126. <https://doi.org/10.1002/2016gl068009>
- Buesseler, K., Lamborg, C., Boyd, P., Lam, P., Trull, T., Bidigare, R., et al. (2007). Revisiting carbon flux through the ocean's twilight zone. *Science*, 316(5824), 567–570. <https://doi.org/10.1126/science.1137959>
- Burd, A., Hansell, D., Steinberg, D., Anderson, T., Arístegui, J., Baltar, F., et al. (2010). Assessing the apparent imbalance between geochemical and biochemical indicators of meso- and bathypelagic biological activity: What is wrong with present calculations of carbon budgets? *Deep Sea Research Part II: Topical Studies in Oceanography*, 57(16), 1557–1571. <https://doi.org/10.1016/j.dsrr.2010.02.022>
- Chelton, D., Deszoeke, R., Schlaak, M., Naggar, K., & Siwertz, N. (1998). Geographical variability of the first baroclinic rossby radius of deformation. *Journal of Physical Oceanography*, 28(3), 28–460. [https://doi.org/10.1175/1520-0485\(1998\)028<0433:gvotfb>2.0.co;2](https://doi.org/10.1175/1520-0485(1998)028<0433:gvotfb>2.0.co;2)
- Coatanoan, C. (2021). Mixed layer depth in the North Atlantic Ocean. Product Information Document (PIDoc). <https://doi.org/10.13155/79588>
- D'Asaro, E., Shecherbina, A., Klymak, J., Molemaker, J., Novelli, G., Guigand, C., et al. (2018). Ocean convergence and the dispersion of flotsam. *Proceedings of the National Academy of Sciences*, 115(6), 1162–1167. <https://doi.org/10.1073/pnas.1718453115>
- Deuser, W., Muller-Karger, F., Evans, R., Brown, O., Esaias, W., & Feldman, G. (1990). Surface-ocean color and deep-ocean carbon flux: How close a connection? Deep sea research Part A. *Oceanographic Research Papers*, 37(8), 1331–1343.
- Deuser, W., Muller-Karger, F., & Hemleben, C. (1988). Temporal variations of particle fluxes in the deep subtropical and tropical north Atlantic: Eulerian versus Lagrangian effects. *Journal of Geophysical Research*, 93(C6), 6857. <https://doi.org/10.1029/jc093ic06p06857>
- Deuser, W., & Ross, E. (1980). Seasonal change in the flux of organic carbon to the deep Sargasso Sea. *Nature*, 283(5745), 364–365. <https://doi.org/10.1038/283364a0>
- Dever, M., Nicholson, D., Oman, M., & Mahadevan, A. (2021). Size-differentiated export flux in different dynamical regimes in the ocean. *Global Biogeochemical Cycles*, 35(3). <https://doi.org/10.1029/2020gb006764>
- Erickson, Z., & Thompson, A. (2018). The seasonality of physically driven export at submesoscales in the northeast Atlantic Ocean. *Global Biogeochemical Cycles*. <https://doi.org/10.1029/2018gb005927>
- Falkowski, P., Barber, R., & Smetacek, V. (1998). Biogeochemical controls and feedbacks on ocean primary production. *Science*, 281(5374), 200–206. <https://doi.org/10.1126/science.281.5374.200>
- Guidi, L., Calil, P., Duhamel, S., Björkman, K., Doney, S., Jackson, G., et al. (2012). Does eddy-eddy interaction control surface phytoplankton distribution and carbon export in the north Pacific subtropical gyre? *Journal of Geophysical Research*, 117(G2). <https://doi.org/10.1029/2012jg001984>
- Guidi, L., Stommel, L., Legendre, L., Picheral, M., Prieur, L., & Gorsky, G. (2007). Vertical distribution of aggregates (.110 mm) and mesoscale activity in the northeastern Atlantic: Effects on the deep vertical export of surface carbon. *Limnology and Oceanography*, 52(1), 7–18. <https://doi.org/10.4319/lo.2007.52.1.00007>
- Gula, J., & Collin, J. (2021). Pyicles: A Python/Fortran hybrid parallelized code for 3D Lagrangian particles advection using ROMS/CROCO model data. Zenodo. <https://doi.org/10.5281/zenodo.4973786>

- Hartman, S., Larkin, K., Lampitt, R., Lankhorst, M., & Hydes, D. (2010). Seasonal and inter-annual biogeochemical variations in the porcupine abyssal plain 2003–2005 associated with winter mixing and surface circulation. *Deep Sea Research Part II: Topical Studies in Oceanography*, 57(15), 1303–1312. <https://doi.org/10.1016/j.dsrr.2010.01.007>
- Henson, S., Yool, A., & Sanders, R. (2015). Variability in efficiency of particulate organic carbon export: A model study: Variability in export ratio. *Global Biogeochemical Cycles*, 29(1), 33–45. <https://doi.org/10.1002/2014gb004965>
- Iversen, M., & Lampitt, R. (2020). Size does not matter after all: No evidence for a size-sinking relationship for marine snow. *Progress in Oceanography*, 189, 102445. <https://doi.org/10.1016/j.pocean.2020.102445>
- Klein, P., & Lapeyre, G. (2009). The oceanic vertical pump induced by mesoscale and submesoscale turbulence. *Annual Review of Marine Science*, 1(1), 351–375. <https://doi.org/10.1146/annurev.marine.010908.163704>
- Kostadinov, T., Siegel, D., & Maritorena, S. (2009). Retrieval of the particle size distribution from satellite ocean color observations. *Journal of Geophysical Research*, 114(C9), C09015. <https://doi.org/10.1029/2009jc005303>
- LaCasce, J. (2008). Statistics from Lagrangian observations. *Progress in Oceanography*, 77(1), 1–29. <https://doi.org/10.1016/j.pocean.2008.02.002>
- Lampitt, R., & Antia, A. (1997). Particle flux in deep seas: Regional characteristics and temporal variability. *Deep Sea Research Part I: Oceanographic Research Papers*, 44(8), 1377–1403. [https://doi.org/10.1016/S0967-0637\(97\)00020-4](https://doi.org/10.1016/S0967-0637(97)00020-4)
- Lampitt, R., Salter, I., de Cuevas, B., Hartman, S., Larkin, K., & Pebody, C. (2010). Long-term variability of downward particle flux in the deep northeast atlantic: Causes and trends. *Deep Sea Research Part II: Topical Studies in Oceanography*, 57(15), 1346–1361. <https://doi.org/10.1016/j.dsrr.2010.01.011>
- Laurenceau-Cornec, E., Le Moigne, F. C., Gallinari, M., Moriceau, B., Toullec, J., Iversen, M., et al. (2020). New guidelines for the application of Stokes' models to the sinking velocity of marine aggregates. *Limnology & Oceanography*, 65(6), 1264–1285. <https://doi.org/10.1002/lno.11388>
- Le Cann, B. (2005). Observed mean and mesoscale upper ocean circulation in the midlatitude northeast atlantic. *Journal of Geophysical Research*, 110(C7), C07S05. <https://doi.org/10.1029/2004jc002768>
- Le Corre, M., Gula, J., & Tréguier, A.-M. (2020). Barotropic vorticity balance of the north atlantic subpolar gyre in an eddy-resolving model. *Ocean Science*, 16(2), 451–468. <https://doi.org/10.5194/os-16-451-2020>
- Le Moigne, F. A. C., Henson, S. A., Sanders, R. J., & Madsen, E. (2013). Global database of surface ocean particulate organic carbon export fluxes diagnosed from the 234th technique. *Earth System Science Data*, 5(2), 295–304. <https://doi.org/10.5194/essd-5-295-2013>
- Lerman, A., Lal, D., & Dacey, M.F. (1974). Stokes' settling and chemical reactivity of suspended particles in natural waters. In R.J. Gibbs, (Ed.), *Suspended solids in water* (Vol. 4). Springer.
- Lévy, M., Ferrari, R., Franks, P., Martin, A., & Rivière, P. (2012). Bringing physics to life at the submesoscale. *Geophysical Research Letters*, 39(14), L14602. <https://doi.org/10.1029/2012gl052756>
- Lévy, M., Franks, P., & Smith, K. (2018). The role of submesoscale currents in structuring marine ecosystems. *Nature Communications*, 9(1), 4758. <https://doi.org/10.1038/s41467-018-07059-3>
- Lévy, M., Jahn, O., Dutkiewicz, S., & Follows, M. (2014). Phytoplankton diversity and community structure affected by oceanic dispersal and mesoscale turbulence: Dispersal impact on plankton diversity. *Limnology and Oceanography: Fluids and Environments*, 4(1), 67–84. <https://doi.org/10.1215/21573689-2768549>
- Liu, G., Bracco, A., & Passow, U. (2018). The influence of mesoscale and submesoscale circulation on sinking particles in the northern gulf of Mexico. *Elementa: Science of the Anthropocene*, 6(1), 36. <https://doi.org/10.1525/elementa.292>
- Mahadevan, A. (2016). The impact of submesoscale physics on primary productivity of plankton. *Annual Review of Marine Science*, 8(1), 161–184. <https://doi.org/10.1146/annurev-marine-010814-015912>
- Mahadevan, A., & Tandon, A. (2006). An analysis of mechanisms for submesoscale vertical motion at ocean fronts. *Ocean Modelling*, 14(3–4), 241–256. <https://doi.org/10.1016/j.ocemod.2006.05.006>
- Martin, A., Boyd, P., Buesseler, K., Cetinic, I., Claustré, H., Giering, S., et al. (2020). Study the twilight zone before it is too late. *Nature*, 580(7801), 26–28. <https://doi.org/10.1038/d41586-020-00915-7>
- McGillicuddy, D. (2016). Mechanisms of physical-biological-biogeochemical interaction at the oceanic mesoscale. *Annual Review of Marine Science*, 8(1), 125–159. <https://doi.org/10.1146/annurev-marine-010814-015606>
- McGillicuddy, D., Robinson, A., & McCarthy, J. (1995). Coupled physical and biological modelling of the spring bloom in the North Atlantic (ii): Three dimensional bloom and post-bloom processes. *Deep Sea Research Part I: Oceanographic Research Papers*, 42(8), 1359–1398. [https://doi.org/10.1016/0967-0637\(95\)00035-5](https://doi.org/10.1016/0967-0637(95)00035-5)
- McWilliams, J. (2008). The nature and consequences of oceanic eddies. In M. Hecht & H. Hasumi (Eds.) *Geophysical monograph series* (Vol. 177, pp. 5–15). American Geophysical Union.
- Olson, D. (1991). Rings in the ocean. *Annual Review of Earth and Planetary Sciences*, 19(1), 283–311. <https://doi.org/10.1146/annurev.ea.19.050191.001435>
- Pidcock, R., Martin, A., Allen, J., Painter, S., & Smeed, D. (2013). The spatial variability of vertical velocity in an Iceland basin eddy dipole. *Deep Sea Research Part I: Oceanographic Research Papers*, 72, 121–140. <https://doi.org/10.1016/j.dsri.2012.10.008>
- Pietri, A., Capet, X., d'Ovidio, F., Levy, M., Le Sommer, J., Molines, J.-M., & Giordani, H. (2021). Skills and limitations of the adiabatic omega equation: How effective is it to retrieve oceanic vertical circulation at mesoscale and submesoscale? *Journal of Physical Oceanography*, 51(3), 931–954. <https://doi.org/10.1175/jpo-d-20-0052.1>
- Pilo, G., Oke, P., Coleman, R., Rykova, T., & Ridgway, K. (2018). Patterns of vertical velocity induced by eddy distortion in an ocean model: Vertical velocity and eddy distortion. *Journal of Geophysical Research: Oceans*, 123(3), 2274–2292. <https://doi.org/10.1002/2017jc013298>
- Poje, A., Haza, A., Özgökmen, T., Magaldi, M., & Garraffo, Z. (2010). Resolution dependent relative dispersion statistics in a hierarchy of ocean models. *Ocean Modelling*, 31(1–2), 36–50. <https://doi.org/10.1016/j.ocemod.2009.09.002>
- Poje, A., Ozgokmen, T., Lippardt, B., Haus, B., Ryan, E., Haza, A., et al. (2014). Submesoscale dispersion in the vicinity of the deepwater horizon spill. *Proceedings of the National Academy of Sciences*, 111(35), 12693–12698. <https://doi.org/10.1073/pnas.1402452111>
- Qiu, Z., Doglioni, A., & Carliotti, F. (2014). Using a Lagrangian model to estimate source regions of particles in sediment traps. *Science China Earth Sciences*, 57(10), 2447–2456. <https://doi.org/10.1007/s11430-014-4880-x>
- Riley, J., Sanders, R., Marsay, C., Le Moigne, F., Achterberg, E., & Poultou, A. (2012). The relative contribution of fast and slow sinking particles to ocean carbon export: Export of fast and slow sinking POC. *Global Biogeochemical Cycles*, 26(1). <https://doi.org/10.1029/2011gb004085>
- Rudnick, D. L. (2001). On the skewness of vorticity in the upper ocean. *Geophysical Research Letters*, 28(10), 2045–2048. <https://doi.org/10.1029/2000gl012265>
- Sanders, R., Henson, S., Koski, M., De La Rocha, C., Painter, S., Poultou, A., et al. (2014). The biological carbon pump in the north atlantic. *Progress in Oceanography*, 129, 200–218. <https://doi.org/10.1016/j.pocean.2014.05.005>

- Shchepetkin, A., & McWilliams, J. (2005). The regional oceanic modeling system (roms): A split-explicit, free-surface, topography-following-coordinate oceanic model. *Ocean Modelling*, 9(4), 347–404. <https://doi.org/10.1016/j.ocemod.2004.08.002>
- Siegel, D., Buesseler, K., Behrenfeld, M., Benitez-Nelson, C., Boss, E., Brzezinski, M., et al. (2016). Prediction of the export and fate of global ocean net primary production: The exports science plan. *Frontiers in Marine Science*, 3. <https://doi.org/10.3389/fmars.2016.00022>
- Siegel, D., & Deuser, W. (1997). Trajectories of sinking particles in the sargasso sea: Modeling of statistical funnels above deep-ocean sediment traps. *Deep Sea Research Part I: Oceanographic Research Papers*, 44(9–10), 1519–1541. [https://doi.org/10.1016/s0967-0637\(97\)00028-9](https://doi.org/10.1016/s0967-0637(97)00028-9)
- Siegel, D., Fields, E., & Buesseler, K. (2008). A bottom-up view of the biological pump: Modeling source funnels above ocean sediment traps. *Deep Sea Research Part I: Oceanographic Research Papers*, 55(1), 108–127. <https://doi.org/10.1016/j.dsr.2007.10.006>
- Siegel, D., Granata, T., Michaels, A., & Dickey, T. (1990). Mesoscale eddy diffusion, particle sinking, and the interpretation of sediment trap data. *Journal of Geophysical Research*, 95(C4), 5305. <https://doi.org/10.1029/jc095ic04p05305>
- Siegelman, L., Klein, P., Rivière, P., Thompson, A., Torres, H., Flexas, M., & Menemenlis, D. (2020). Enhanced upward heat transport at deep submesoscales ocean fronts. *Nature Geoscience*, 13(1), 50–55. <https://doi.org/10.1038/s41561-019-0489-1>
- Stukel, M., Aluwihare, L., Barbeau, K., Chekalyuk, A., Goericke, R., Miller, A., et al. (2017). Mesoscale ocean fronts enhance carbon export due to gravitational sinking and subduction. *Proceedings of the National Academy of Sciences*, 114(6), 1252–1257. <https://doi.org/10.1073/pnas.1609435114>
- Taylor, J. R., Smith, K. M., & Vreugdenhil, C. A. (2020). The influence of submesoscales and vertical mixing on the export of sinking tracers in large-eddy simulations. *Journal of Physical Oceanography*, 50(5), 1319–1339. <https://doi.org/10.1175/jpo-d-19-0267.1>
- Thomas, L. N., Tandon, A., & Mahadevan, A. (2008). Submesoscale processes and dynamics. In M. W. Hecht & H. Hasumi (Eds.), *Geophysical Monograph Series* (Vol. 177, pp. 17–38). American Geophysical Union.
- Trull, T., Bray, S., Buesseler, K., Lamborg, C., Manganini, S., Moy, C., & Valdes, J. (2008). In situ measurement of mesopelagic particle sinking rates and the control of carbon transfer to the ocean interior during the vertical flux in the global ocean (vertigo) voyages in the north Pacific. *Deep Sea Research Part II: Topical Studies in Oceanography*, 55(14–15), 1684–1695. <https://doi.org/10.1016/j.dsr2.2008.04.021>
- Turner, J. (2002). Zooplankton fecal pellets, marine snow and sinking phytoplankton blooms. *Aquatic Microbial Ecology*, 27, 57–102. <https://doi.org/10.3354/ame027057>
- Turner, J. (2015). Zooplankton fecal pellets, marine snow, phytodetritus and the ocean's biological pump. *Progress in Oceanography*, 130, 205–248. <https://doi.org/10.1016/j.pocean.2014.08.005>
- Vic, C., Gula, J., Roullet, G., & Pradillon, F. (2018). Dispersion of deep-sea hydrothermal vent effluents and larvae by submesoscale and tidal currents. *Deep Sea Research Part I: Oceanographic Research Papers*, 133, 1–18. <https://doi.org/10.1016/j.dsr.2018.01.001>
- Vic, C., Hascoët, S., Gula, J., Huck, T., & Maes, C. (2022). Oceanic mesoscale cyclones cluster surface Lagrangian material. *Geophysical Research Letters*, 49(4), e2021GL097488. <https://doi.org/10.1029/2021gl097488>
- Villa-Alfageme, M., de Soto, F., Le Moigne, F. A. C., Giering, S. L. C., Sanders, R., & García-Tenorio, R. (2014). Observations and modeling of slow-sinking particles in the twilight zone. *Global Biogeochemical Cycles*, 28(11), 1327–1342. <https://doi.org/10.1002/2014gb004981>
- Waite, A., Stemann, L., Guidi, L., Callil, P., Hogg, A., Feng, M., et al. (2016). The wineglass effect shapes particle export to the deep ocean in mesoscale eddies: The wineglass effect. *Geophysical Research Letters*, 43(18), 9791–9800. <https://doi.org/10.1002/2015gl066463>
- Waniek, J., Koeve, W., & Priest, R. (2000). Trajectories of sinking particles and the catchment areas above sediment traps in the northeast Atlantic. *Journal of Marine Research*, 58(6), 983–1006. <https://doi.org/10.1357/002224000763485773>
- Wekerle, C., Krumpen, T., Dinter, T., von Appen, W.-J., Iversen, M., & Salter, I. (2018). Properties of sediment trap catchment areas in fram strait: Results from Lagrangian modeling and remote sensing. *Frontiers in Marine Science*, 5, 407. <https://doi.org/10.3389/fmars.2018.00407>
- Yu, X., Naveira Garabato, A., Martin, A., Buckingham, C., Brannigan, L., & Su, Z. (2019). An annual cycle of submesoscale vertical flow and restratification in the upper ocean. *Journal of Physical Oceanography*, 49(6), 1439–1461. <https://doi.org/10.1175/jpo-d-18-0253.1>
- Zhang, Z., Qiu, B., Klein, P., & Travis, S. (2019). The influence of geostrophic strain on oceanic ageostrophic motion and surface chlorophyll. *Nature Communications*, 10(1), 2838. <https://doi.org/10.1038/s41467-019-10883-w>